



# Development of a large nanocrystalline soft magnetic alloy core with high $\mu'_p Qf$ products for CSNS-II

Bin Wu<sup>1,2</sup> · Xiao Li<sup>1,2</sup> · Zhun Li<sup>1,2</sup> · Chun-Lin Zhang<sup>1,2</sup> · Yang Liu<sup>1,2</sup> · Wei Long<sup>1,2</sup> · Xiang Li<sup>1,2,3</sup> · Jian Wu<sup>1,2,3</sup>

Received: 28 February 2022 / Revised: 11 June 2022 / Accepted: 25 June 2022 / Published online: 16 August 2022

© The Author(s), under exclusive licence to China Science Publishing & Media Ltd. (Science Press), Shanghai Institute of Applied Physics, the Chinese Academy of Sciences, Chinese Nuclear Society 2022

**Abstract** A waterproof nanocrystalline soft magnetic alloy core with a size of O.D.850 mm × I.D.316 mm × H.25 mm for radio frequency acceleration was successfully developed by winding 18  $\mu\text{m}$  1k107b MA ribbons. The  $\mu'_p Qf$  products reached 7.5, 10, and 12 GHz at 1, 3, and 5 MHz, respectively. The  $\mu'_p Qf$  products of the MA core (O.D.250 mm × I.D.100 mm × H.25 mm) manufactured using a 13  $\mu\text{m}$  MA ribbon further increased by 30%. Detailed improvements on the MA core manufacture process are discussed herein. Continuous high-power tests on the new MA cores demonstrated its good performance of waterproofness, particularly its stability of high  $\mu'_p Qf$  products. The MA core with high  $\mu'_p Qf$  product and large size can operate under a high average RF power, high electric field, and in deionized water, which will be used in the China Spallation Neutron Source Phase II (CSNS-II).

**Keywords** Large size magnetic alloy core · High insulation and low stress coating · Waterproof structure · Transverse magnetic field annealing · High power MA-loaded cavity

## 1 Introduction and background

The nanocrystalline soft magnetic alloy (MA) has the characteristics of a high saturation flux density, high permeability, and high Curie temperature [1], enabling it to be widely used in common mode chokes, radio-frequency (RF) switching power supplies, and microwave absorption [2]. In recent years, the MA core prepared by winding MA ribbons has been used as an inductance loading material in coaxial resonant cavities to achieve a high acceleration gradient and wide operating frequency band; it has become a key technology for high-power proton/heavy ion synchrotrons such as the Japanese Proton Accelerator (J-PARC) and the Proton and Antiproton Research Device (FAIR) [3, 4]. Compared with the traditional coaxial resonant cavity loaded with ferrite cores, the MA-loaded cavity can have a smaller volume, wider operating band range, and higher acceleration gradient. The long-term stability of the entire RF system is significantly improved as a complex tuning system is not required for MA-loaded cavity.

An increase in the proton beam power from 100 to 500 kW is planned for the rapid cycle synchrotron (RCS) of the China Spallation Neutron Source Phase II Project (CSNS-II). Three MA-loaded cavities will be installed in the RCS to dilute the space charge effect of the proton beam and increase the beam capture efficiency [5]. According to the beam dynamics design, the MA-loaded

This work was supported by the funds of the National Natural Science Foundation of China (Nos. 11175194, 11875270, and U1832210), Youth Innovation Promotion Association CAS (No. 2018015), and Guangdong Basic and Applied Basic Research Foundation (No. 2019B1515120046).

✉ Bin Wu  
wubin@ihep.ac.cn

✉ Xiao Li  
lixiao@ihep.ac.cn

<sup>1</sup> Institute of High Energy Physics, Chinese Academy of Sciences, Beijing 100049, China

<sup>2</sup> Spallation Neutron Source Science Center, Dongguan 523803, China

<sup>3</sup> University of Chinese Academy of Sciences, Beijing 100049, China

cavity must provide the fundamental and second harmonic voltages. The average power density of the MA cores will exceed  $0.3 \text{ W/cm}^3$ , and the maximum acceleration gradient of the MA-loaded cavity will be up to  $40 \text{ kV/m}$ . A direct cooling method was adopted for MA cooling [6]. Table 1 shows the comparison of RF parameters of the MA loaded cavity in CSNS-II/RCS and J-PARC [3, 7].

However, when the MA-loaded cavity operates under a high electric field gradient and high average power density, local ignition, ablation, and deformation may occur in the MA core owing to the problems of interlayer insulation breakdown and increase in eddy current loss [8]. Therefore, the MA core should be especially fabricated, such as treating the MA ribbon with an insulation layer, increasing MA core size and applying a magnetic field during annealing, and encapsulating the MA core for special cooling environments. However, these special treatments will increase the internal stress of MA materials, resulting in a decrease in the high-frequency characteristics of the MA core [9]. Currently, MA cores with high performance and large size that can operate under a high average power, a high electric field gradient, and in water are produced by Hitachi LTD, Japan [10], but the MA cores and core preparation technology are subject to a technical blockade and embargo owing to export control laws.

In this study, with respect to the application requirements of CSNS-II/RCS, the key technologies to prepare a large-size and high-performance MA core using domestic MA ribbon were studied. The second part of this paper introduces the research in detail, including the development of high insulation and low stress coating, large MA core winding and transverse magnetic field annealing, as well as the waterproof curing encapsulation of the MA core. The research results are evaluated and discussed. The third part describes the building of a high-power test system to evaluate the stability of the new MA cores under actual operating conditions for 31 days.

## 2 Fabrication of high- $\mu'_p Qf$ product and large MA cores

A high-performance MA core is primarily characterized by a high shunt impedance and long-time operation under a high-average-power-density and high-electric-field-gradient environment. The shunt impedance of the MA core determines the acceleration gradient of the MA-loaded cavity and the maximum average power density that it can operate with Eq. (1). Increasing the shunt impedance ( $R_p$ ) is beneficial to reducing the power loss ( $P$ ) of the cavity under the condition of constant voltage ( $U_{rf}$ ), which makes the entire RF system more energy saving and stable. Additionally, the cavity length can even be shortened to increase the acceleration gradient.

$$U_{rf} = \sqrt{2PR_p} \tag{1}$$

However,  $R_p$  is proportional to the  $\mu'_p Qf$  product and geometry factor ( $A$ ), which are defined by Eqs. (2) and (3) [7]. The  $\mu'_p Qf$  product is an important parameters for an RF cavity; it is the product of  $Q$  and  $\mu'_p$  and the operating frequency  $f$ , where  $Q$  and  $\mu'_p$  are the quality factor and real part of the parallel permeability of the loaded material, respectively.

$$R_p = (\mu'_p Qf) \cdot A, \tag{2}$$

$$A = \mu_0 \cdot \ln\left(\frac{r_2}{r_1}\right) \cdot d \cdot n \cdot F, \tag{3}$$

where  $r_1$  and  $r_2$  are the inner and outer radius, respectively, of the MA core with a thickness of  $d$ ,  $\mu_0$  is the vacuum permeability,  $n$  is the number of MA cores used, and  $F$  is the lamination coefficient of the MA core, which is defined as the proportion of the area of the MA ribbon to the total area in the radial section of the MA core. According to the parameters in Table 1, the CSNS-II/RCS MA-loaded cavity are suitable for high power and high gradient applications, the  $\mu'_p Qf$  product of the MA core should be as high as

**Table 1** Comparison of RF parameters of high power and high gradient MA cavities of CSNS-II/RCS and J-PARC

	CSNS-II/RCS	J-PARC/RCS	J-PARC/MR
Length of cavity (m)	1.8	1.95	2.591
Number of accelerating gap	3/cavity	3/cavity	5/cavity
Max. accelerating gradient (kV/m)	40	21	32
Working band (MHz)	1–8	1–5	1.718
Size of MA core (mm <sup>3</sup> )	φ850 × φ316 × 25	φ854 × φ375 × 35	φ800 × φ245 × 25
Average power density (W/cm <sup>3</sup> )	> 0.3	0.37	0.8
Type of cooling	Direct cooling	Direct cooling	Direct cooling
Coolant	Deionized water	Deionized water	Deionized water
Type of MA material	1k107B	FINEMET	FINEMET

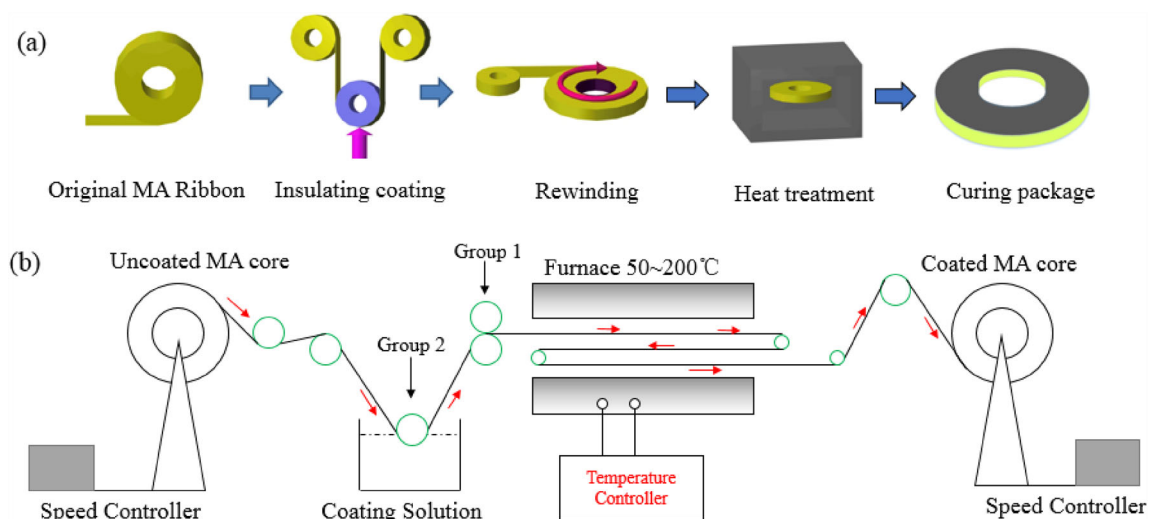
possible, and an MA core with a large size and high lamination-coefficient is preferred. For the MA core to operate under a high-power and high-electric-field-gradient environment, the MA ribbon should be coated to avoid the adjacent layer ignition from breaking down, and the MA core should be encapsulated to adapt to deionized water (at 25 °C) for sufficient cooling. Under the condition that the MA core can satisfy the engineering application, the problem of reducing the influence of the preparation process on the MA core magnetic property also should be solved.

The key processes of a MA core manufacture are shown in Fig. 1a. In this study, an MA ribbon with a width of 25 mm and thickness of about 18  $\mu\text{m}$  was used; the model was 1k107B with the composition of  $\text{Fe}_{84}\text{Cu}_1\text{Nb}_{5.5}\text{Si}_{8.2}\text{B}_{1.3}$  (at%) and provided by Advanced Technology & Materials Co., Ltd. (AT&M). To prevent the MA material from being oxidized during the annealing process, we added an inert gas to the annealing furnace for protection.

## 2.1 Insulation treatment of MA ribbon surface

Four types of coating method were studied. The advantages and disadvantages are summarized in Table 2. Only the  $\text{SiO}_2$  coating prepared using the sol-gel process satisfied the requirement of low stress and high insulation used for high-performance MA core fabrication. Figure 1b shows the sol-gel coating facility and process. The thickness of the wet film was controlled by controlling the spacing of Group 1 rollers. Three small rollers were installed in the oven to prolong the standing time of the ribbon to ensure that the surface of the MA ribbon was completely dried before winding.

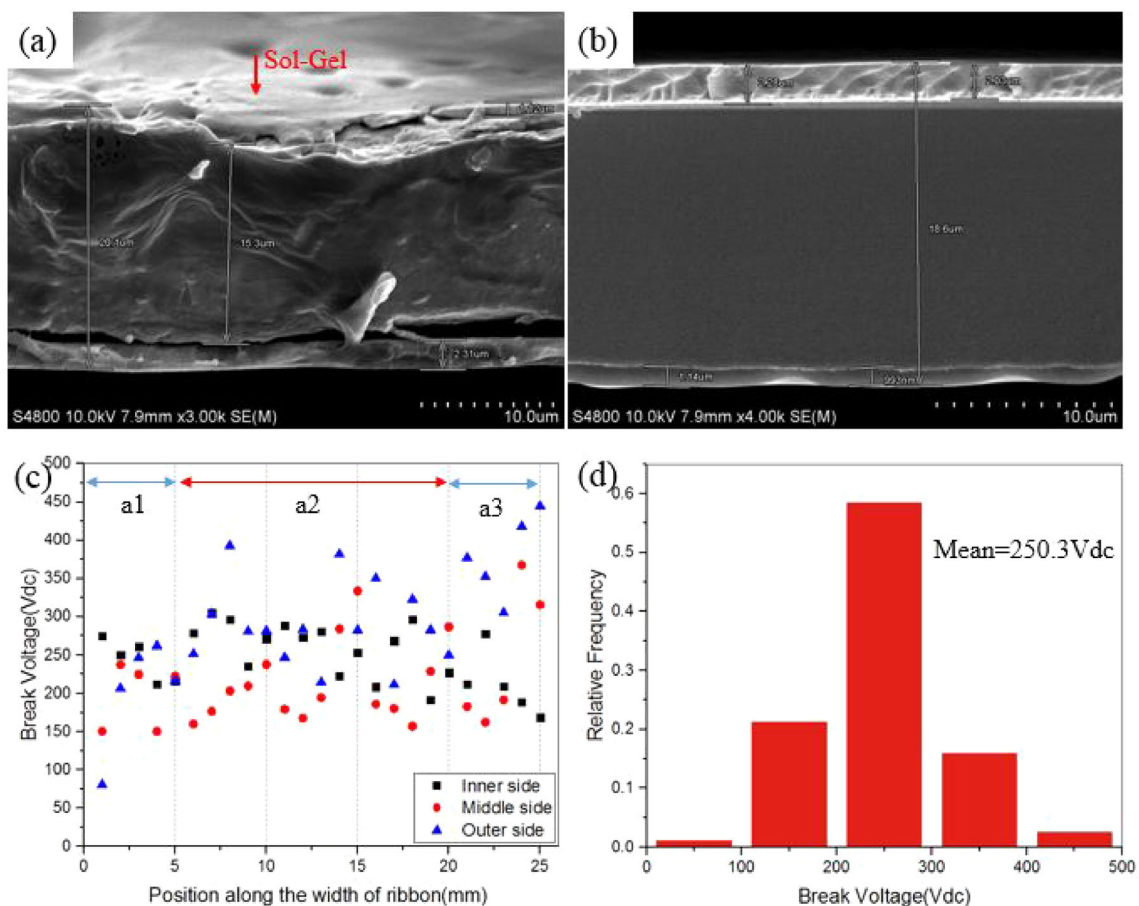
Figure 2a and b shows the cross-sectional observation of the sol-gel/ $\text{SiO}_2$  coating on the MA ribbon before and after annealing, respectively, using a Hitachi S-3400 N high-resolution scanning electron microscope. Before annealing, the sol-gel film was a coating with an irregular morphology, and the element proportions of Si and O were 50.33% and 37.07%, respectively. A dense  $\text{SiO}_2$  inorganic coating was formed with an average thickness of about 2  $\mu\text{m}$  after the annealing at 500–600 °C (Fig. 2b). The element proportions of Si and O were 50.85% and 35.99%, respectively, which were consistent with the element proportions before annealing, indicating that the sol-gel/ $\text{SiO}_2$  coating had good thermal stability. An insulation tester (Fluke 1550C) was used to test the voltage hold-off on the annealed MA ribbon. The selected positions of the MA ribbon samples were located at the inner diameter, middle, and the outer diameter areas of the MA core, as shown by the symbols B1, B2, and B3, respectively, in Fig. 3a. Testing was conducted along the 2.5 cm width of the MA ribbon. The results of the inner, middle, and outer regions are indicated by the black, red, and blue scatters, respectively, in Fig. 2c. The symbols a1 and a3 represent the areas 5 mm away from the edge of the MA ribbon, and a2 represents the middle region. The average breakdown voltages of regions a1, a2, and a3 were 214, 253, and 278 Vdc, respectively. Figure 2d shows a histogram of the frequency statistics of all the results. The test data satisfied the Gaussian distribution, whose median and mean were 247 and 250.3 Vdc, respectively. The MA core used in the CSNS-II/RCS MA-loaded cavity has a lamination coefficient of 0.75. According to its definition, the induced RF voltage is about 2 V with the ribbon spacing of 6  $\mu\text{m}$  [15]. The test results indicated that the developed sol-gel/ $\text{SiO}_2$  coating can satisfy the RF voltage insulation requirement



**Fig. 1** (Color online) Key processes of manufacturing high-performance MA cores **a**; Sol-gel coating facility and process **b**

**Table 2** Comparison of different coating methods for the insulating treatment of the MA core

Coating method	Insulation materials	Softening temperature	Advantages	Disadvantages
Physical deposition[11]	MgO	650 °C	Coating easily; low cost	Low adhesion; moisture absorption; low insulation
IBAD[12]	SiO, SiO <sub>2</sub>	1600 °C	High insulation; thin in depth;	High cost; low efficiency
PHPS[13]	SiO <sub>2</sub>	1600 °C	High insulation; thin in depth;	Strong stress
Sol-gel[14]	SiO <sub>2</sub>	1600 °C	High insulation; thin in depth; low stress	Coating crack

**Fig.2** (Color online) Cross sections of the sol-gel coating on the surface of the MA ribbon before and after annealing **a** and **b**; Ultimate breakdown voltage of the samples in the different regions of MA core **c**; Frequency statistics of all ultimate breakdown voltage measurements **d**

of CSNS-II/RCS MA core and with a sufficient engineering margin.

A thermal shock experiment was performed on the coated MA ribbon to evaluate the possibility of coating cracking in long-term engineering use, as the difference

between the thermal expansion coefficients of SiO<sub>2</sub> and MA ribbon was large, which were about  $3 \times 10^{-6}/\text{K}$  and  $10.6 \times 10^{-6}/\text{K}$ , respectively [16]. The coated MA ribbon samples with a length of 5 cm were heated from room temperature to 120 °C within 3 min; the ribbon was

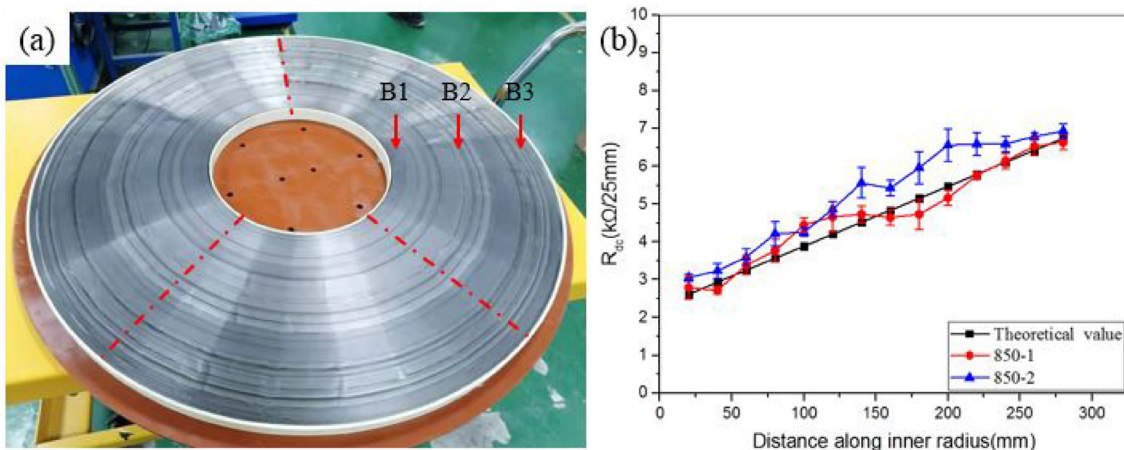


**Fig. 3** (Color online) Appearance of the MA core with the size of O.D.850 mm × I.D.316 mm × H.25 mm after annealing **a**; Comparison of the measured and theoretical values of radial DC resistance of the MA core **b**

maintained at 120 °C for 1 h, and then, it was cooled to room temperature within 3 min. This process was repeated 200 times. The results showed that the appearance of the MA ribbon coating was complete without apparent peeling off, and the insulation performance and energy-dispersive spectroscopy element ratio of the MA ribbon coating were almost the same as those before the thermal shock test, which further proved the excellent thermal stability and adhesion of the sol-gel/SiO<sub>2</sub> coating.

The effects of coating on the RF performance of the MA core were also evaluated by winding MA cores of different sizes. An SY-8232 type IWATSU B-H analyzer was used to measure the RF loss ( $P_{cv}$ ), and the average  $\mu'_p Qf$  products were measured using a vector network analyzer. The measurement methods and theoretical derivation of the  $\mu'_p Qf$  product are introduced in [17]. The detail test condition and results are listed in Table 3. The results showed that the average RF loss of the coated MA cores was significantly lower than the un-coated MA cores (CK), and the  $\mu'_p Qf$  products of the coated-MA core increased by about 30% at 1, 3, and 5 MHz. These results confirmed that the sol-gel/SiO<sub>2</sub> coating has lower stress and can effectively reduce the high-frequency eddy current loss and improve the  $\mu'_p Qf$  products of the MA core.

### 2.2 Large MA core winding

A horizontal winding process was adopted for a large and high-filling-factor MA core winding instead of the traditional vertical winding process, which causes significant damage to the MA ribbon coating [18]. The weight of the MA core was evenly distributed on the support back-plane, and the tension required for the MA core winding was significantly reduced. The ribbon tension was kept as low and constant as possible to ensure that the stress distribution of each layer of the MA core was uniform by dynamically adjusting the rotational speed of the unwinding and rewinding motors. In addition, we developed a multi-core lap joint process. A large MA core was composed of several small coated MA cores as the front end of the last roll was mounted on the back end of the first roll.

Figure 3a shows a MA core with a size of O.D.850 mm × I.D.316 mm × H.25 mm after winding. We measured the radial resistance of the MA core using a digital multimeter to evaluate whether the inter-layer insulating coating of the MA core was peeled off after winding [18]. To reduce the measurement error, we measured three path lines on the end face of the MA core at 120° intervals along the core circumferential direction, as shown by the three red dotted lines in Fig. 2a. The average

**Table 3** RF properties of MA cores with or without coating treatments

Test condition	Dynamic magnetic property		$\mu'_p Qf$ products (GHz)		
	$B_m = 200$ mT, 100 kHz $\phi 25$ mm × $\phi$ 10 mm × 25 mm		$\phi 450$ mm × $\phi 200$ mm × 25 mm		
	Sol-gel/SiO <sub>2</sub>	CK	Fre (MHz)	Sol-gel/SiO <sub>2</sub>	CK
$P_{cv}$ (kW/m <sup>3</sup> )	177.65	232.35	1	4.06	2.86
			3	5.78	3.97
			5	6.87	4.57

Note: All MA core were annealed without a magnetic field

value of the three lines at each the 25-mm interval points were considered the final radial resistance measurement results. Figure 3b shows a comparison of the radial resistance distribution of the two MA cores denoted as “850–1” and “850–2” and their theoretical values, in which “Theoretic value” is the theoretical calculation value of the radial resistance in the assumption that the inter-layer insulation of the MA core is good. We observed that the measured results could be better distributed near the theoretical value, which demonstrated that the horizontal winding process has minimal influence on the coating of the MA ribbon [18]. We also observed that the results could completely coincide with the theoretical value. The main reason is that the thickness and resistivity of the MA ribbon fluctuated typically within the range of  $\pm 5\%$  during production, and a measurement error was also introduced.

### 2.3 MA core annealing with a transverse magnetic field

A segmented pre-annealing process was developed to solve the problems of temperature lag and overshoot in the large MA core during the annealing process [19]. This method is beneficial to maintaining a good follow-up between the temperature change of the MA core and the preset temperature of the annealing furnace and gradually releasing the amorphous latent heat. Additionally, a static magnetic field was applied parallel to the axial direction of the center of the MA core during the annealing process to improve the  $\mu_p'Qf$  product of the MA core [20].

Figure 4 shows the  $\mu_p'Qf$  products of the MA core developed in this study and a comparison with the J-PARC

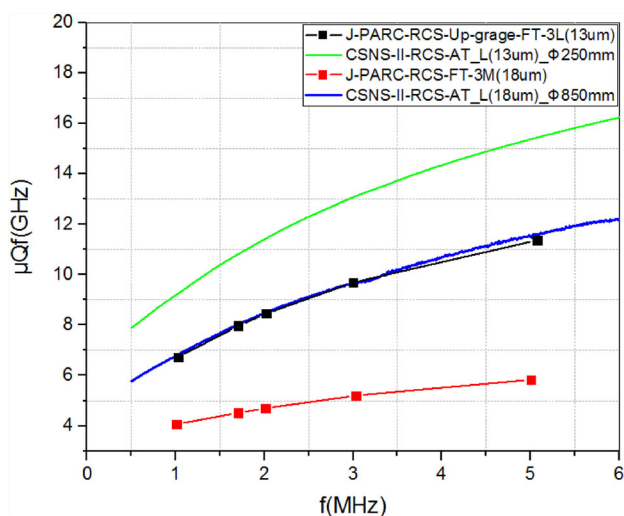


**Fig. 4** (Color online) Comparison of the  $\mu_p'Qf$  products of the developed and J-PARC MA cores

MA core [7]. The abscissa is the measured frequency range of 0.5–6 MHz, and the ordinate is the  $\mu_p'Qf$  product in GHz. The red scatter line in Fig. 4 is the performance level of the MA core with the size of O.D.854 mm  $\times$  I.D.375 mm  $\times$  H.35 mm currently used in J-PARC/RCS. It was prepared using an 18  $\mu\text{m}$  FINEMET MA ribbon with a  $\text{SiO}_2$  coating of about 2  $\mu\text{m}$  and without a transverse magnetic field process, denoted as FT-3 M (18  $\mu\text{m}$ ). The  $\mu_p'Qf$  products were about 4, 5.5, and 6.5 GHz at 1, 3, and 5 MHz, respectively. The  $\mu_p'Qf$  products were improved to 6.9, 10.2, and 12 GHz at 1, 3, and 5 MHz, respectively, after the ribbon thickness was reduced to 13  $\mu\text{m}$  and a transverse magnetic field was applied during the annealing process [7], indicated as FT-3L (13  $\mu\text{m}$ ) by the black scatter line in Fig. 4. Note that the  $\mu_p'Qf$  products of the developed domestic MA core with the size of O.D.850 mm  $\times$  I.D.316 mm  $\times$  H.25 mm prepared using the 18  $\mu\text{m}$  1k107B MA ribbon was close to FT-3L (13  $\mu\text{m}$ ), as shown by the blue solid line in Fig. 4. It is now in the stage of mass production and will be used in CSNS-II/RCS. As expected, the  $\mu_p'Qf$  products can be further improved by using a 13  $\mu\text{m}$  MA ribbon [21]. For the experimental MA core with a size of O.D.250 mm  $\times$  I.D.100 mm  $\times$  H.25 mm, the  $\mu_p'Qf$  products further increased to 9.2, 13, and 15 GHz at 1, 3, and 5 MHz, respectively, as shown by green solid line in Fig. 4. However, we observed a phenomenon in which when the 13  $\mu\text{m}$  1K107 MA ribbon was used to prepare a MA core with larger size, only about 80% of the performance of small core could be achieved. The reason has not been determined yet, but it may be explained by the quality instability of 13  $\mu\text{m}$  MA ribbon mass production in domestic factories and the change in the crystallization thermodynamic behavior in the thin MA ribbon. The annealing and magnetization process of thin MA ribbon wound core remains to be further studied, but it will become the optimization objective of domestic higher-performance and large MA cores in the future.

### 2.4 MA core waterproof package

An epoxy curing encapsulation process is often adopted to avoid the long-term erosion to the MA core by water [8]. However, the cured epoxy resin has a large stress, which results in a large decrease in the high-frequency performance of the MA core. Through numerical simulation and experiments, Morita et al. confirmed that the epoxy resin infiltrating an MA core is what generates a strong stress in the circumferential direction under a high temperature [8, 16]. Therefore, we designed a new type of packaging structure that can effectively prevent the epoxy resin from

infiltrating the interior of MA core. The packaging structure is described as follows: The inner and outer diameter of the MA core is supported by a fiberglass-reinforced tube with a thickness of about 3 mm. The first layer on the end face of the MA core is a coating containing large particles of SiO<sub>2</sub> with a thickness of about 50 μm to fill the tiny gap between the MA ribbons, preventing the subsequent penetration of epoxy into the interior of MA core. Additionally, it provides a good insulation on the MA core end face. The second layer is a cured layer formed by high viscosity epoxy resin and glass fiber cloth, and its main function is to preliminarily shape the MA core. The final layer is a leveling layer formed by the curing of low-concentration epoxy resin and fiberglass cloth; thus, the MA core has sufficient mechanical strength and is waterproof while smoothing the MA core surface. The low-concentration epoxy wraps the entire MA core during curing, and the inner and outer diameter corners of the MA core will also be sufficiently protected. The entire curing process was completed in a vacuum chamber. After curing, the total thickness of the encapsulation layer was less than 1 mm, the thermal conductivity was about 0.5 W/m/K, and the maximum temperature resistance of the encapsulation layer was about 150 °C. Figure 5a shows the appearance of the MA core after packaging.

Because the MA material is sensitive to the stress, the infiltration of epoxy resin and water into the interior of MA core causes a change in the  $\mu'_p Qf$  products [22]. We evaluated whether epoxy resin or water penetrates the MA core by measuring the change in the  $\mu'_p Qf$  product of the MA core in each curing process and a waterproof test. The  $\mu'_p Qf$  product of the MA core after annealing is shown by the black rectangle solid line in Fig. 5b. After the first layer of SiO<sub>2</sub> treatment, the maximum decrease ratio of the  $\mu'_p Qf$

product in the range of 1–10 MHz was less than 2%. The reason was that the thickness of the SiO<sub>2</sub> coating was about 50 μm, which induced a certain stress on the end face of the MA core, but the effect was small. After the epoxy resin cured and encapsulated, the  $\mu'_p Qf$  products had almost no change, which indicated that the epoxy resin had not penetrated the MA core, as shown by the blue upper triangle solid line. After packaging, the MA core was immersed in circulating deionized water at 25 °C for 30 days, and the water pressure was maintained at 0.3 MPa (simulating an actual operating environment). The  $\mu'_p Qf$  products remained stable, which is indicated by the pink lower triangle solid line in Fig. 5b. The encapsulation layer on the surface of the MA core was complete and had no apparent color change. The experimental results preliminarily confirmed that the MA core had a good waterproofing ability.

Similar to the MA ribbon coating, a thermal shock experiment was performed as the thermal expansion coefficient of epoxy resin in the encapsulation layer was  $60 \times 10^{-6}/K$ , which was six times higher than the thermal expansion coefficient of the MA material. There would be a risk of stress fatigue in the encapsulated MA core. The encapsulated MA core was placed in an oven as the temperature varied from 25 to 120 °C within 10 min, maintained for 2 h, and finally cooled to the room temperature within 10 min. This process was repeated 100 times. The experimental results showed that the appearance and the  $\mu'_p Qf$  products of the MA core had no apparent changes after the thermal shock test. This proved that the encapsulation layer had a significant hardness and adhesion. The waterproof performance and transient thermal shock resistance of the MA core encapsulation layer will also be

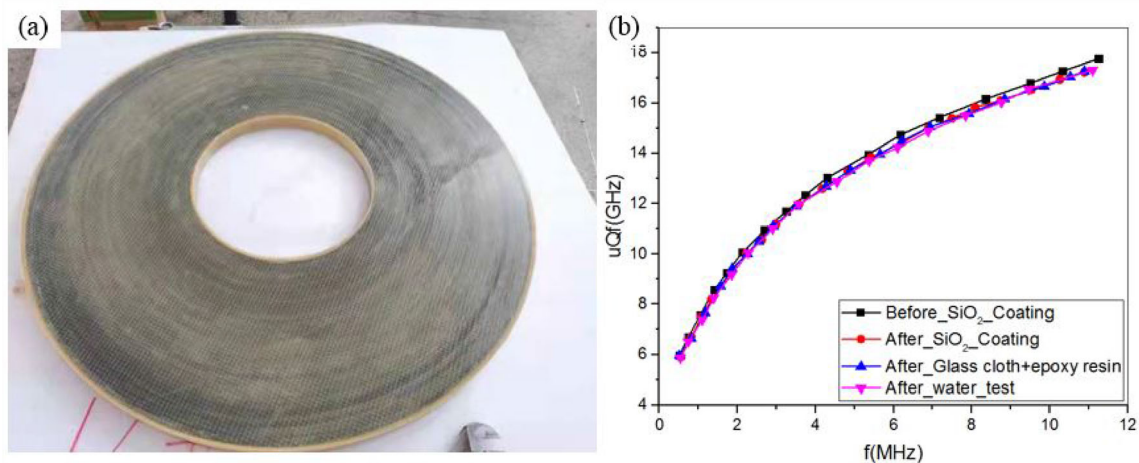


**Fig. 5** (Color online) Appearance of the MA core after waterproof curing and encapsulation **a**. Comparison of the  $\mu'_p Qf$  product of MA core in each process of packaging

evaluated in subsequent high-power tests under actual operating conditions.

### 3 MA core test platform and continuous high power testing

A schematic of the high-power test system of the MA core is shown in Fig. 6a. The test system included a single-gap MA test cavity, RF power source, a low-level RF control system (LLRF), and temperature-monitoring system. The two sides of the ceramic acceleration gap in the middle of the MA-loaded cavity were two water tanks. Each tank could simultaneously cool three MA cores with the size of O.D.850 mm × I.D.316 mm × H.25 mm. Owing to the large size of the MA core, a deflector was installed between the MA cores to reduce backflow. The RF power required by the cavity was directly fed using an RF power source composed of two TH558 high-power tetrode tubes connected to the metal rings on both sides of the ceramic through the feeding copper bar. The operating mode of the two RF power sources was PUSH-PULL, which meant that the voltages  $\tilde{V}_1$  and  $\tilde{V}_2$  on both sides of the gap had the same amplitude, but the phase difference was 180°. The amplitude and phase were closed-loop

controlled using the LLRF. The two RF power sources would observe the impedance of the respective half-cavities; the entire test system was equivalent to the parallel equivalent circuit in Fig. 6b. The two power sources were equivalent to current sources  $I_{g1}$  and  $I_{g2}$ , the distributed capacitance including the cavity and water is  $C_p$ .  $L_p$  and  $R_p$  are the parallel equivalent inductance and shunt impedance of the MA core,  $n$  is the number of half-cavity used MA cores, and  $C_{gap}$  is the capacitance of the ceramic gap, which was about 34 pF.

The high-power test of the MA core under the average power density of 0.33 W/cm<sup>3</sup> was performed using the second-harmonic voltage sweeping mode used for CSNS-II/RCS. Figure 6c shows the voltage amplitudes measured with the LLRF on one side of the ceramic gap. The frequency range was from 1.5 to 2.6 MHz, and the duty cycle was 15% under the condition of a 50 Hz repetition frequency. Because the TH558 high-power tetrode tubes operated in the AB1 class mode, the gap voltage contained the components of higher harmonics. Through fast Fourier analysis, we observed that the maximum voltage amplitude of the fundamental component on each tank reached 12 kV, the maximum voltage amplitude of the second and third harmonic components reached 3 and 0.5 kV, respectively, as shown by red and blue solid lines in

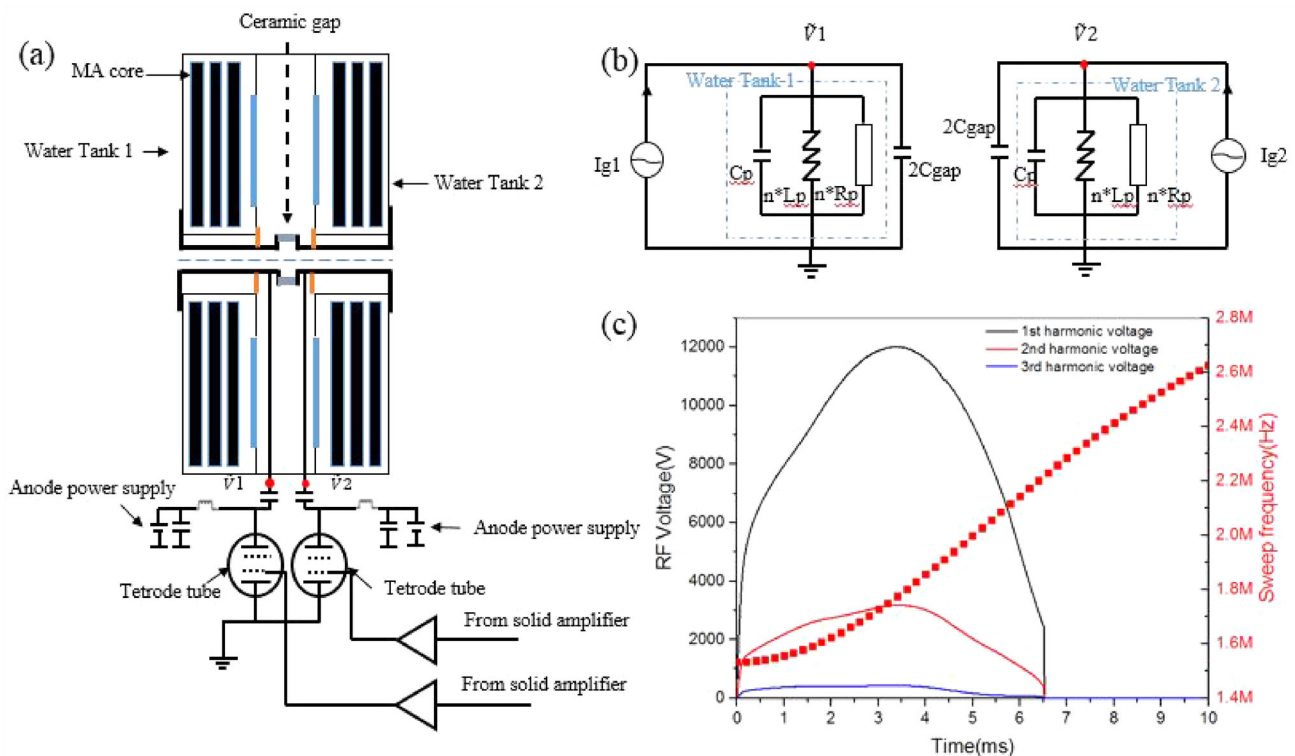


**Fig. 6** (Color online) Schematic of the MA core high power test system **a**; Equivalent circuit of MA cavity test system **b**; The amplitudes of the fundamental, second, and third harmonics are

represented by black, red, and blue solid lines, respectively, the cavity operating frequency variation is represented by red scatters, and the amplitudes correspond to the right red axis in **c**

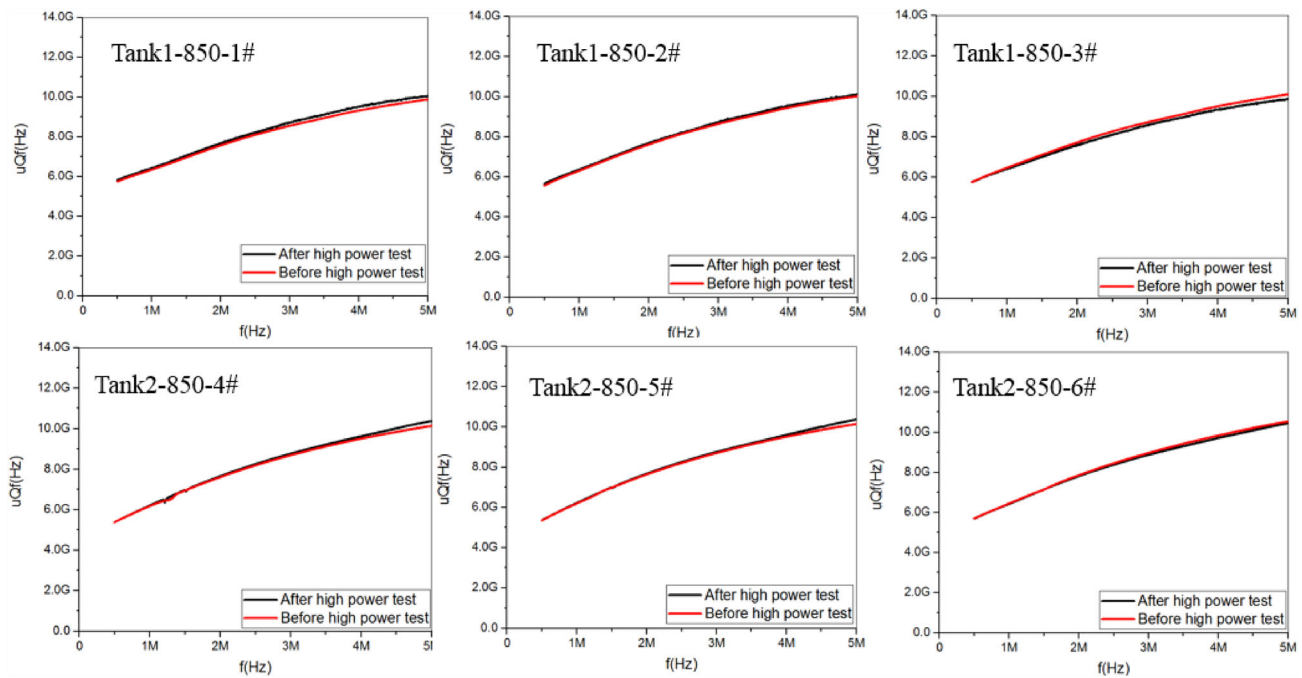


**Fig. 7** Comparison of the  $\mu'_p Qf$  product of MA cores before and after a 31-day high-RF power test with an average power density of  $0.33 \text{ W/cm}^3$  and maximum accelerating gradient of  $40 \text{ kV/m}$ . The

MA cores 850-1#, 850-2#, and 850-3# were located in Tank 1 and the remainder were in Tank 2

Fig. 6c. The maximum fundamental voltage synthesized by the gap was  $24 \text{ kV}$ . The cavity acceleration gradient was  $40 \text{ kV/m}$  with a cavity length of  $0.6 \text{ m}$ . Owing to the low  $Q$  value of the MA cores, the power loss of the cavity was primarily concentrated in the MA core of the tank; thus, the power loss of the MA cores could be calculated by measuring the water temperature difference between the outlet and inlet of the tank and water flow rate. According to the theory of coaxial resonant cavity, the MA cavity length was much smaller than the wavelength of the cavity operating frequency (about  $20 \text{ m}$  at  $1 \text{ MHz}$ ); therefore, the power losses of each MA core in the tank were almost equal. The thermal power calculation formula of the tank is shown in Eq. (4) [15], where  $\Delta T$  is the water temperature difference between the inlet and outlet of the tank. The temperature probes were high-precision PT100 thermocouples with a measurement error of  $\pm 0.001 \text{ }^\circ\text{C}$ ;  $L$  is the water flow of the cavity, taken as  $L = 40 \text{ L/min}$ ;  $\rho$  is the water density, taken as  $997 \text{ kg/m}^3$  at  $30 \text{ }^\circ\text{C}$ ;  $C$  is the specific heat capacity of water, taken as  $4181.7 \text{ J/kg/K}$  at  $30 \text{ }^\circ\text{C}$ .

$$P_{\text{measurement}} = \Delta T \cdot L \cdot \rho \cdot C \quad (4)$$

Six MA cores with the size of  $\text{O.D.}850 \text{ mm} \times \text{I.D.}316 \text{ mm} \times \text{H.}25 \text{ mm}$  were installed in the tanks for the high-RF power test under the voltage mode for 31 days (Fig. 6c). The water temperature at the inlet of the tank was about  $24.5 \text{ }^\circ\text{C}$ . Under the condition that the thermal power

loss was  $12 \text{ kW}$  in each tank, the outlet water temperature was about  $28.4 \text{ }^\circ\text{C}$ . During the test period, owing to the ignition of the cavity gap sampling module, the LLRF protected the RF power system five times, and the total accumulated shutdown time was less than  $1 \text{ h}$ . The protection action of the LLRF can be used as a thermal shock test for the MA cores. Figure 7 compares the  $\mu'_p Qf$  products of six MA cores before and after the high-power test indicated by red and black solid lines; the abscissa is the frequency range of  $0.5\text{--}5 \text{ MHz}$ , and the ordinate is the measured  $\mu'_p Qf$  product in Hz. We observed that the largest decrease in the  $\mu'_p Qf$  product of MA cores was less than  $3\%$ , and the appearance of the MA cores after high power test remained the same as earlier. The results indicated that the MA core had a good stability under high power, high accelerating gradient, and in water. A longer time of the high power test will be conducted.

## 4 Conclusion

In this study, aiming at the application requirements of CSNS-II/RCS, a waterproof and large MA core with high  $\mu'_p Qf$  products was prepared using domestic MA ribbons. The  $\mu'_p Qf$  products of the MA cores in the stage of mass production reached the performance level of the MA core

used in J-PARC. To ensure the long-term stable operation of the MA core in CSNS-II, we conducted performance evaluation tests at every step of the preparation of MA core. The continuous high-power tests under the actual operating conditions demonstrated the stability and water-proofness of the  $\mu_p Qf$  products.

**Author contributions** All authors contributed to the study conception and design. Material preparation, data collection and analysis were performed by Bin Wu, Chun-Lin Zhang, Yang Liu, Xiang Li, Jian Wu and Zhun Li. The first draft of the manuscript was written by Bin Wu and all authors commented on previous versions of the manuscript. All authors read and approved the final manuscript.

## References

1. K. Suzuki, A. Makino, A. Inoue et al., Soft magnetic properties of nanocrystalline bcc Fe-Zr-B and Fe-M-B-Cu (M=transition metal) alloys with high saturation magnetization (invited). *J. Appl. Phys.* **70**(10), 6232–6237 (1991). <https://doi.org/10.1063/1.350006>
2. Y.H. Lv, J. Zhang, B. Li et al., Mössbauer spectroscopy studies on the particle size distribution effect of Fe-B-P amorphous alloy on the microwave absorption properties. *Nucl. Sci. Tech.* **31**(3), 24 (2020). <https://doi.org/10.1007/s41365-020-0734-8>
3. M. Yamamoto, K. Hasegawa, M. Yoshii et al., High power test of MA cavity for J-PARC RCS. In: 2007 IEEE Particle Accelerator Conference (PAC). 1532–1534 (2007). <https://doi.org/10.1109/PAC.2007.4440813>
4. T. Trupp, NANOPERM broad band magnetic alloy cores for synchrotron RF systems. IPAC (2014). <https://doi.org/10.18429/JACoW-IPAC2014-MOPRO016>
5. B. Wu, H. Sun, X. Li et al., Higher harmonic voltage analysis of magnetic-alloy cavity for CSNS/RCS upgrade project. *Radiat. Detect. Technol. Method* **4**, 293–302 (2020). <https://doi.org/10.1007/s41605-020-00183-z>
6. T. Uesugi, Y. Mori, C. Ohmori et al., Direct-cooling MA cavity for J-PARC synchrotrons. In: Proceedings of the 2003 Particle Accelerator Conference, pp. 1234–1236 (2003). <https://doi.org/10.1109/PAC.2003.1289663>
7. C. Ohmori, E. Ezura, K. Hara et al., Development of a high gradient rf system using a nanocrystalline soft magnetic alloy. *Phys. Rev. ST Acc. Beams* **16**(11), 112002 (2013). <https://doi.org/10.1103/physrevstab.16.112002>
8. M. Nomura, M. Yamamoto, A. Schnase et al., The origin of magnetic alloy core buckling in J-PARC 3GeV RCS. *Nucl. Instrum. Meth. A* **623**(3), 903–909 (2010). <https://doi.org/10.1016/j.nima.2010.08.111>
9. R.K. Nutor, X. Fan, S. Ren et al., Research progress of stress-induced magnetic anisotropy in Fe-based amorphous and nanocrystalline alloys. *J. Electromagn. Anal. App.* **09**(4), 53–72 (2017). <https://doi.org/10.4236/jemaa.2017.94006>
10. P. Hulsmann, G. Hutter, W. Vinzenz, The bunch compressor system for SIS18 AT GSI. In: Proceedings of EPAC2004, Lucerne, Switzerland, pp. 1165–1167 (2004).
11. X. Zhou, S. Li, J. Li et al., Preparation of special silicon steel grade MgO from hydromagnesite. *J. Univ. Sci. Technol. Beijing Miner. Metall. Mater.* **14**(3), 225–230 (2007). [https://doi.org/10.1016/S1005-8850\(07\)60043-7](https://doi.org/10.1016/S1005-8850(07)60043-7)
12. J.M. Choi, H.E. Kim, I.S. Lee, Ion-beam-assisted deposition (IBAD) of hydroxyapatite coating layer on Ti-based metal substrate. *Biomaterials* **21**(5), 469–473 (2000). [https://doi.org/10.1016/S0142-9612\(99\)00186-6](https://doi.org/10.1016/S0142-9612(99)00186-6)
13. K. Sato, H. Kaya, O. Funayama et al., Evaluation of polysilazanes-perhydropolysilazane, polyborosilazane and methylhydropolysilazane as matrix precursors of ceramic-matrix composites. *J. Ceram. Soc. Jpn.* **109**, 440–446 (2001). [https://doi.org/10.2109/jcersj.109.1269\\_440](https://doi.org/10.2109/jcersj.109.1269_440)
14. S.H. Lim, Y.S. Choi, Effects of surface coating by sol-gel process on the magnetic properties of a Co-based amorphous alloy. *Magn. IEEE Trans.* **31**(6), 3898–3900 (1995). <https://doi.org/10.1109/20.489809>
15. Y. Morita, T. Kageyama, Development of medium-frequency cavity loaded with multi-ring magnetic alloy cores cooled by chemically inert liquid. *Nucl. Instrum. Meth. A* **1010**, 165525 (2021). <https://doi.org/10.1016/j.nima.2021.165525>
16. Y. Morita, T. Kageyama, M. Akoshima et al., Numerical analysis and experiment to identify origin of buckling in rapid cycling synchrotron core. *Nucl. Instrum. Meth. A* **728**, 23–30 (2013). <https://doi.org/10.1016/j.nima.2013.05.177>
17. K. Wang, Z. Xu, P. Jin et al., Design of the deceleration magnetic alloy cavity for a high-intensity heavy-ion accelerator facility spectrometer ring. *Nucl. Instrum. Meth. A* **1005**, 165364 (2021). <https://doi.org/10.1016/j.nima.2021.165364>
18. M. Nomura, A. Schnase, T. Shimada et al., A convenient way to find an electrical insulation break of MA cores in J-PARC synchrotrons. *Nucl. Instrum. Meth. A* **668**, 83–87 (2011). <https://doi.org/10.1016/j.nima.2011.11.092>
19. J. He, K.Y. He, L.Z. Cheng et al., The influence of pre-annealing treatment on the exothermic behavior and magnetic properties of Fe<sub>73.5</sub>Cu<sub>1</sub>Nb<sub>3</sub>Si<sub>13.5</sub>B<sub>9</sub> alloy. *J. Magn. Magn. Mater.* **208**, 44–48 (2000). [https://doi.org/10.1016/S0304-8853\(99\)00550-8](https://doi.org/10.1016/S0304-8853(99)00550-8)
20. M. Nomura, T. Shimada, F. Tamura et al., Mechanisms of increasing of the magnetic alloy core shunt impedance by applying a transverse magnetic field during annealing. *Nucl. Instrum. Meth. A* **797**, 196–200 (2015). <https://doi.org/10.1016/j.nima.2015.06.061>
21. M. Nomura, T. Shimada, F. Tamura et al., Ribbon thickness dependence of the magnetic alloy core characteristics in the accelerating frequency region of the J-PARC synchrotrons. *Nucl. Instrum. Meth. A* **749**, 84–89 (2014). <https://doi.org/10.1016/j.nima.2014.02.041>
22. E. Ezura, M. Nomura, K. Hasegawa et al., Condition of MA Cores in the RF cavities of J-PARC synchrotrons after several years of operation. In: Proceedings of IPAC'10, Kyoto, Japan, THPEA022, pp. 3723–3725 (2010).

Springer Nature or its licensor holds exclusive rights to this article under a publishing agreement with the author(s) or other rightsholder(s); author self-archiving of the accepted manuscript version of this article is solely governed by the terms of such publishing agreement and applicable law.